Length-Scale Correction for Reynolds Stress Modeling

Bernhard Eisfeld *
DLR Braunschweig, Lilienthalplatz 7, D-38108 Braunschweig, Germany

Christopher L. Rumsey. †
NASA Langley Research Center, MS 128, Hampton, VA, USA

A length-scale correction term is developed for the SSG/LRR-ω Reynolds-stress model that is based on an analysis of the Yap correction. The model with and without the correction is implemented into two flow solvers and applied to four flows featuring separation. The length-scale correction increases the negative skin friction within separation bubbles and moves the reattachment point downstream. It remedies the unphysical back-bending of streamlines near reattachment that has been observed with the original model.

Nomenclature

A	Coefficient of length-scale correction
b_{ij}	Cartesian component of the anisotropy tensor
$C_D^{(\omega)}$	Cross-diffusion of ω, m^2/s^4
C_i	Coefficients of pressure-strain correlation
C_i^*	Coefficients of pressure-strain correlation
C_l	Coefficient of Yap correction
C_p	Pressure coefficient
ΔC_p	Shift in pressure coefficient
$C_{\epsilon 2}$	Coefficient of ϵ-destruction
c	Chord length, m
$c_2^{(LRR)}$	Coefficient of pressure-strain correlation (LRR-model)
c_f	Local skin friction coefficient
c_μ	Coefficient for ϵ/ω conversion
D_{ij}	Cartesian component of Reynolds-stress diffusion tensor, m^2/s^3
$D^{(GD)}$	Coefficient of generalized gradient diffusion model
$D^{(\epsilon)}$	Diffusion of ϵ, m^2/s^4
$D^{(\omega)}$	Diffusion of ω, m^2/s^4

*Research Scientist, Dept. $C^2A^2S^2E$, Institute of Aerodynamics and Flow Technology.
†Research Scientist, Computational AeroSciences Branch, NASA Langley Research Center, MS 128, Hampton, VA, USA, Fellow AIAA.

d	Distance to closest wall, m
d_1	Wall-distance of nearest field point, m
F	Extrapolation factor for ω at walls
F_1	Menter's blending function
$F^{(LSC)}$	Length-scale correction
k	Specific kinetic turbulence energy, m^2/s^2
H	Step height, m
L	Unit length, m
$\mathcal{L}_t$	Turbulent length scale, m
ℓ_{log}	Turbulent length scale in log-layer, m
M	Mach number
N	Grid point or cell number
$P^{(\epsilon)}$	Production of ϵ, m^2/s^4
$P^{(\omega)}$	Production of ω, $1/s^2$
P_{ij}	Cartesian component of Reynolds stress production tensor, m^2/s^3
p	Pressure, Pa
R_{ij}	Cartesian component of specific Reynolds stress tensor, m^2/s^2
	in inner scaling
Re_ℓ	Reynolds number based on length ℓ, with $\ell = c$, H or L
S_{ij}	Cartesian component of strain rate tensor, 1/s
S^*_{ij}	Cartesian component of traceless strain rate tensor, 1/s
$S_l^{(\epsilon)}$	Yap correction in ϵ-equation, m^2/s^4
$S_l^{(\omega)}$	Yap correction transformed to ω-equation, $1/s^2$
T	Temperature, K
Tu_∞	Turbulence intensity at the far field
t	Time, s
U	Streamwise Cartesian velocity component, m/s
U_i	Cartesian component of velocity vector, m/s
W_{ij}	Cartesian component of rotation tensor, 1/s
x	Streamwise Cartesian co-ordinate, m
x_i	Cartesian co-ordinate, m
y	Wall-normal Cartesian co-ordinate, m

y'	Wall-normal Cartesian co-ordinate with origin at the surface, m

Symbols

α	Coefficient of ω production
β	Coefficient of ω destruction
δ	Boundary layer thickness, m
δ_{ij}	Kronecker symbol
ϵ	Isotropic dissipation rate, m^2/s^3
ϵ_{ij}	Cartesian component of dissipation rate tensor, m^2/s^3
ζ	Argument to Menter's blending function F_1
κ	Von Karman constant
μ	Molecular (dynamic) viscosity, kg/(m · s)
μ_t	Equivalent eddy viscosity, kg/(m · s)
Π_{ij}	Cartesian component of pressure-strain correlation, m^2/s^3
ρ	Density, kg/m^3
σ_d	Coefficient of ω cross-diffusion term
σ_ω	Coefficient of ω diffusion term
τ_w	Wall shear stress, $kg/(m{\cdot}s^2)$
$\Phi^{(\epsilon)}$	Destruction of ϵ, m^2/s^4
$\Phi^{(\omega)}$	Destruction of ω, $1/s^2$
χ	Parameter of length-scale correction
χ_T	Threshold value of χ
ω	Specific dissipation rate, 1/s

Subscripts

log	In logarithmic layer
ref	Reference conditions
w	At the wall
∞	At the far field

I. Introduction

Numerical flow simulations have been used for aircraft design for decades. However, the simulations have typically only been considered reliable as long as the flow remains attached, i.e., near cruise conditions. In contrast, the reliability of the simulations is observed to degrade under high-lift conditions or at the edge of the envelope where separated flow dominates. Hence there is an industrial need for improvement.

In principle, scale-resolving methods like Direct Numerical Simulation (DNS) or Large-Eddy Simulation (LES) are supposed to yield accurate results, provided the spatial and temporal resolution is sufficiently fine. However, the required computational effort is still prohibitive for most industrial applications [1]. Hybrid methods like the Detached-Eddy Simulation (DES) [2] and Wall-Modeled LES (WMLES) are beginning to show promising results for aeronautical configurations on grids of a managable size, e. g. [3]. Nevertheless, they still require time-accurate simulations. Therefore, there is a demand for more accurate predictions at least of mildly separating flows based on the Reynolds-averaged Navier-Stokes (RANS) equations, involving a turbulence model [4].

Reynolds stress models provide the highest level of modelling within the RANS context, employing six transport equations for the individual specific Reynolds stresses R_{ij} and an additional transport equation for a length-scale providing variable like the dissipation rate ϵ or the specific dissipation rate ω. Such models are numerically more demanding than classical eddy-viscosity models like the ones by Spalart and Allmaras (SA) [5] or the Shear Stress Transport (SST) model by Menter [6]. Nevertheless, it has been shown that in particular the so-called SSG/LRR-ω model [7, 8], combining the models by Speziale, Sarkar and Gatski (SSG) [9] and of Launder, Reece and Rodi (LRR) [10] with the baseline ω-equation of Menter [6], can be applied to a wide variety of aerodynamic test cases, including complex aircraft configurations with fluid-structure interaction [11–14].

While promising results have been obtained with the SSG/LRR-ω model for a number of test cases, some peculiarities have been observed with separated flows, concerning the level of skin friction in the reverse flow domain and an unphysical back-bending of the streamlines near reattachment [13]. Irregular streamline patterns near reattachment have been previously observed with various Reynolds stress models, e.g., by Obi et al. [15], Lasher and Taulbee [16] and Hanjalić and Jakirlić [17]. The latter authors show that the anomaly can be remedied by an additional source term in the ϵ-transport equation, aimed at reducing the turbulent length scale $\mathcal{L}_t$ [17]. This term has been inspired by a correction originally developed by Yap [18, 19] who observed excessive $\mathcal{L}_t$-values near reattachment.

For this reason, the Yap-correction [18, 19] is revisited and transferred to the transport equation of the specific dissipation rate ω. Interpreting the Yap-correction as a modification of the ω-destruction term, a formulation is developed that improves previous predictions of separating flows with the SSG/LRR-ω model.

II. Yap Correction

A. Original Formulation

Originally, the Yap correction [18, 19] was based on the transport equation for the dissipation rate ϵ, which can be written for the case of a high turbulent Reynolds number as

$$\frac{\partial \epsilon}{\partial t} + U_k \frac{\partial \epsilon}{\partial x_k} = P^{(\epsilon)} - \Phi^{(\epsilon)} + D^{(\epsilon)}, \tag{1}$$

in which $P^{(\epsilon)}$ denotes the production, $D^{(\epsilon)}$ the turbulent diffusion and

$$\Phi^{(\epsilon)} = C_{\epsilon 2} \frac{\epsilon^2}{k} \tag{2}$$

is the destruction of ϵ with $C_{\epsilon 2}$ being a constant coefficient. Yap [18] observed that, near reattachment with this equation, the turbulent length scale

$$\mathcal{L}_t = \frac{k^{3/2}}{\epsilon} \tag{3}$$

exceeds the value of the turbulent length scale in the logarithmic part of a boundary layer

$$\ell_{log} = \frac{k_{log}^{3/2}}{\epsilon_{log}} = c_\mu^{-3/4} \kappa d, \tag{4}$$

in which d is the wall-distance, $\kappa = 0.41$ is the von Kármán constant and $c_\mu = 0.09$. As a consequence, excessive heat transfer rates are predicted near reattachment on cooled or heated walls [19].

In order to reduce the turbulent length scale in this region, Yap added the source term

$$S_l^{(\epsilon)} = \max \left[C_l \frac{\epsilon^2}{k} \left(\frac{\mathcal{L}_t}{\ell_{log}} - 1 \right) \left(\frac{\mathcal{L}_t}{\ell_{log}} \right)^2, 0 \right] \tag{5}$$

to Eq. (1), in which $C_l = 0.83$. Comparison with Eq. (2) reveals that due to the different signs, this correction essentially reduces the ϵ-destruction when the length-scale ratio $\mathcal{L}_t / \ell_{log} > 1$.

B. Transformation to ω-Transport Equation

The SSG/LRR-ω model employs Menter's baseline ω-equation [6]

$$\frac{\partial \omega}{\partial t} + U_k \frac{\partial \omega}{\partial x_k} = P^{(\omega)} - \Phi^{(\omega)} + D^{(\omega)} + C_D^{(\omega)}, \tag{6}$$

in which $P^{(\omega)}$ denotes the production, $D^{(\omega)}$ the viscous and turbulent diffusion and

$$\Phi^{(\omega)} = \beta\omega^2 \tag{7}$$

is the destruction of ω, with β being a coefficient that depends on the distance from the wall. The additional cross-diffusion term $C_D^{(\omega)}$ arises from the formal transformation of the ϵ-diffusion term according to

$$\epsilon = c_\mu k\omega, \tag{8}$$

in which $c_\mu = 0.09$.

The corresponding Yap correction is obtained by rescaling the source term (5) according to

$$S_l^{(\omega)} = \frac{\omega}{\epsilon} S_l^{(\epsilon)} = \max\left[C_l c_\mu \omega^2 \left(\frac{\mathcal{L}_t}{\ell_{log}} - 1\right)\left(\frac{\mathcal{L}_t}{\ell_{log}}\right)^2, 0\right], \tag{9}$$

in which the length-scale ratio is given by

$$\frac{\mathcal{L}_t}{\ell_{log}} = \frac{k^{1/2}}{c_\mu^{1/4}\kappa\omega d}. \tag{10}$$

Comparison with Eq. (7) reveals that the transformed Yap correction (9) can be expressed in terms of the ω-destruction term according to

$$S_l^{(\omega)} = \frac{c_\mu C_l}{\beta}\Phi^{(\omega)} \max\left[\left(\frac{\mathcal{L}_t}{\ell_{log}} - 1\right)\left(\frac{\mathcal{L}_t}{\ell_{log}}\right)^2, 0\right], \tag{11}$$

where in the near-wall region, including the log-layer, $\beta = 0.0747$ [6] so that

$$\frac{c_\mu C_l}{\beta} = 1. \tag{12}$$

Comparison with Eq. (7) confirms that the Yap correction (11) essentially reduces the ω-destruction when length-scale ratios $\mathcal{L}_t/\ell_{\log} > 1$. This is the starting point for developing an appropriate length-scale correction for the SSG/LRR-ω model.

III. Length-Scale Correction

Adding the transformed Yap correction (11) to Menter's baseline ω-equation (6) corresponds to modifying the ω-destruction term according to

$$\Phi^{(\omega)} = (1 - \chi)\,\beta\omega^2, \tag{13}$$

in which the parameter

$$\chi = \max\left[\left(\frac{\mathcal{L}_t}{\ell_{log}} - 1\right)\left(\frac{\mathcal{L}_t}{\ell_{log}}\right)^2, 0\right] \tag{14}$$

follows from Eq. (11).

Figure 1 shows the steep unbounded increase of χ with the length-scale ratio. At $\mathcal{L}_t/\ell_{log} \approx 1.466$, a value of $\chi = 1$ is reached, beyond which the destruction term changes its sign and thus turns into an additional production term. Test computations of flows with separation, using the SSG/LRR-ω model [13, 20] without modification, show maximum length-scale ratios near reattachment of the order of $\mathcal{L}_t/\ell_{log} \approx 2.5$, indicating the sign change in the ω-destruction occurs in realistic applications.

Since in the exact ϵ-transport equation the destruction term is strictly nonnegative, a sign change of the corresponding ω-destruction term is felt to be undesirable. Hence a transformation $F^{(LSC)}(\chi)$ is sought that maps the parameter χ onto the bounded codomain $0 \leq F^{(LSC)}(\chi) \leq 1$. This is achieved by choosing

$$F^{(LSC)}(\chi) = \frac{1}{2}\left\{1 + \tanh\left[A\left(\chi - \chi_T\right)\right]\right\}, \tag{15}$$

in which the parameter χ_T controls the value of χ, where the function $F^{(LSC)}(\chi)$ switches from zero to one, and the coefficient A determines how rapidly this change takes place.

The parameter χ_T is chosen such that the function $F^{(LSC)}(\chi)$ switches at the same value at which, according to the Yap correction, the ω-destruction term would change its sign, i.e., $\chi_T = 1$. The value of the coefficient is set to $A = 31$, ensuring $F^{(LSC)}(\chi_T - 0.1) = 0.002$ and $F^{(LSC)}(\chi_T + 0.1) = 0.998$, respectively, i.e., a rather rapid change in the range $0.9 \leq \chi \leq 1.1$. For comparison, the length-scale correction function $F^{(LSC)}$ is also plotted in Fig. 1, confirming the above considerations. Note the different scales for χ and $F^{(LSC)}$ in Fig. 1.

With this correction, the destruction term of Menter's baseline ω-equation (6) becomes

$$\Phi^{(\omega)} = \left[1 - F^{(LSC)}(\chi)\right]\beta\omega^2, \tag{16}$$

where from now on $F^{(LSC)}(\chi)$ is denoted as the length-scale correction (LSC). The full set of equations of the SSG/LRR-ω model, including the length-scale correction, are given in the Appendix.

IV. Computational Results

A. Computational Method

Numerical computations, employing the SSG/LRR-ω model with and without the length-scale correction, are carried out using DLR's unstructured TAU code [21] and NASA's structured CFL3D code [22, 23]. Both codes solve the compressible RANS equations together with a variety of turbulence model equations based on a finite-volume

approach, employing discretization schemes for the advection terms of second-order accuracy for the mean flow and of first-order accuracy for the turbulence equations. In contrast, the diffusion terms of all equations are discretized equally with a central scheme of second-order accuracy. Both codes allow for time-accurate simulations, employing a dual-time stepping method. Nevertheless, if not indicated otherwise, for the test cases investigated, a steady state solution has been achieved that has converged to near machine accuracy.

B. Test Cases

Four test cases involving flow separation from NASA's Turbulence Modeling Resource (TMR) website[24] have been selected for demonstrating the effect of the developed length-scale correction. This website also provides a series of structured grids. The same grids are used for both TAU and CFL3D. In each of the test cases, the grid level employed was found to be fine enough to reduce discretization errors in both codes to acceptable levels, with resulting code-to-code differences that were small compared to the differences caused by LSC. TAU and CFL3D generally use different default values for freestream turbulence intensity (Tu_∞) and viscosity ratio ($\mu_t/\mu|_\infty$). For the cases here, the CFL3D defaults were used in both codes, but use of TAU's default levels made no perceptible difference in any of the results. The respective values are indicated for each test case individually.

Note, although not shown, the LSC has been checked for the flow over a flat plate, and the length-scale correction indeed is not active. Hence no influence is expected for attached flows.

1. Backward-Facing Step

The flow over a backward-facing step is characterized by a fixed separation location at the corner-point of the step of height H. Downstream of the separation, a shear-layer develops that bends down until reattachment at a distance of approximately $6H$ from the step.

The subsequent simulations refer to the experiments by Driver and Seegmiller [25], using a wind-tunnel with a height before the step of $8H$ and a width of $12H$, minimizing the influence of the lateral walls. The Reynolds number based on the step height of $Re_H = 36{,}000$ ensures a fully turbulent boundary layer at the step of thickness $\delta = 1.5H$. The Mach number of $M = 0.128$ represents nearly incompressible flow. The experimental data are provided on the TMR website [24].

The computational domain is comprised of an inflow channel of $110H$ length and $8H$ height upstream of the step followed by a $50H$ long and $9H$ high downstream section. The inflow channel is preceded by a section of $20H$ length with symmetry conditions instead of viscous walls. Figure 2 shows a sketch of the computational domain[24].

The grid provided on the TMR website [24] consists of four structured blocks with altogether $N = 319{,}468$ cells on the second finest level that have been fused together for use in the unstructured TAU code. At the inlet plane, a turbulence intensity of $Tu_\infty = 0.061\%$ and a viscosity ratio of $\mu_t/\mu|_\infty = 0.009$ are assumed, following CFL3D defaults.

At the outlet, the pressure is set consistent with the specified reference Mach number. The reference temperature is set to $T_{ref} = 318.33K$ according to the TMR website [24]. With TAU, a steady state has been reached, whereas with CFL3D the solution remained unsteady and had to be computed in time-accurate mode. In the following comparisons, CFL3D results refer to time-averaged data.

Figure 3 shows the distributions of the pressure coefficient $C_p = (p - p_{ref})/(\frac{1}{2}\rho_{ref}U_{ref}^2)$ and the skin-friction coefficient $c_f = \tau_w/(\frac{1}{2}\rho_{ref}U_{ref}^2)$. Note that, according to the TMR website [24], the reference pressure p_{ref} has been defined such that $C_p = 0$ at position $x/H = 40$ downstream of the step. As one can see, there is virtually no influence of LSC on the pressure distribution, whereas the skin-friction is noticeably modified. The recirculation region, indicated by negative values of c_f, is increased, moving the reattachment point from $x/H \approx 5.78 \ldots 5.79$ without length-scale correction to $x/H \approx 6.25$, which almost perfectly matches the experimental reattachment location at $x/H = 6.26 \pm 0.10$. Even though within the recirculation zone the experimental level of negative c_f is not fully reached, LSC yields very good agreement with the experimental data downstream of reattachment. Note also the good agreement between the steady-state TAU results and the time-averaged CFL3D results, indicating only a weak time-dependence of the solution.

Figure 4 shows profiles of the streamwise velocity and the Reynolds-shear stress at four different positions in the range $1 \leq x/H \leq 10$, i.e., covering the recirculation zone. Interestingly, the improvement in skin-friction prediction is accompanied by very little change in the velocity profiles. Differences between the predictions with and without the length-scale correction are limited to a shallow area close to the wall and do not significantly alter the velocity profiles. Again, the agreement between the steady-state TAU results and the time-averaged CFL3D results is good, except for some differences in the recirculation region at $x/H = 1$.

The corresponding Reynolds-shear stress profiles obtained with and without the length-scale correction also show only very minor differences, which are best recognized close to the respective extrema. Since the length-scale correction increases the dissipation, the magnitudes of the maxima are reduced. In this case, the CFL3D results have been omitted because only time-dependent Reynolds-stress data are available. Hence, a slightly larger deviation from the steady-state TAU results is observed that would shadow the small effect of the length-scale correction.

Figure 5 shows the steady-state streamline pattern in the recirculation region obtained by TAU with and without the length-scale correction. Clearly, without the correction, the streamlines bend backward close to the reattachment, whereas the correction provides a smoother shape of the streamlines. The shaded area indicates where the length-scale correction is active. This region extends downstream to $x/H \approx 16$, which is therefore not fully shown. Note that the normal direction in Fig. 5 is enlarged relative to the streamwise direction, in order to improve the visibility of the flow pattern.

Table 1 NASA-hump. Measured and predicted locations of separation and reattachment in terms of x/c.

	Experiment	SSG/LRR-ω without LSC	SSG/LRR-ω with LSC	Spalart & Allmaras [5]	Menter SST [6]
Separation	0.665	0.654	0.654	0.660	0.653
Reattachment	1.1	1.18	1.23 – 1.25	1.27 – 1.28	1.25 – 1.27

2. NASA-Hump

The two-dimensional flow over a wall-mounted hump (NASA-hump), involving pressure induced separation has been studied experimentally by Greenblatt et al. [26–28]. The flow conditions are defined by a Reynolds number of $Re_c = 936{,}000$, based on the chord length c of the hump, and an inflow Mach number of $M = 0.1$. At the inlet plane, a turbulence intensity of $Tu_\infty = 0.077\%$ and a viscosity ratio of $\mu_t/\mu|_\infty = 0.009$ are assumed, following CFL3D defaults. According to the TMR website [24], the reference temperature is $T_{ref} = 298.3K$. Figure 6 shows a sketch of the geometry of the NASA-hump, indicating the boundary conditions [24].

In the experiment, the hump did not span the entire wind-tunnel width, but had end plates for enforcing the two-dimensionality of the flow over the hump. In numerical simulations, the blockage effect of these end plates is usually modeled by a contoured top wall, setting slip-wall conditions [1]. In the current study, the finest grid from the TMR website[24] has been employed with $N = 210{,}060$ grid points after removing the plenum chamber, originally included for simulating flow control.

Figure 7 shows the pressure and skin-friction distributions obtained with the SSG/LRR-ω model with and without length-scale correction in comparison with the experimental data of Greenblatt et al. [26–28] provided on the TMR website [24]. As on the TMR website [24], the C_p-data of the simulations have been shifted by $\Delta C_p = -0.015$ to better match the experimental reference upstream. There is generally good agreement between TAU and CFL3D results, where the largest differences are observed in c_f downstream of the reattachment point.

Similar to the backward-facing step case, the length-scale correction has very little influence on the pressure distribution, but clearly changes the skin friction. As with the backward-facing step, the level of negative c_f is slightly increased, and the reattachment location, indicated by $c_f = 0$, is moved further downstream. Contrary to the backward-facing step case, the length-scale correction is worsening the agreement with the experimental data in this case. Nevertheless, comparing with the results for other models compiled from the TMR website [24] in Table 1, this behavior is typical of RANS models. It should be noted that this test case poses considerable difficulties even for Large-Eddy Simulations [1].

Figure 8 shows the streamline pattern in the recirculation region, where the normal direction has been enlarged compared to the streamwise direction for improved visibility. As with the backward-facing step, the length-scale correction suppresses the back-bending of the streamlines near reattachment. The shaded area indicates where the

length-scale correction is active. This region extends downstream to $x/c \approx 2.4$ and is therefore not fully shown.

3. Axisymmetric Bump

The transonic flow over a cylinder with an axisymmetric bump has been experimentally investigated by Bachalo and Johnson [29]. The flow conditions are defined by a Reynolds number of $Re_c = 2.763 \times 10^6$ based on the chord length c of the bump and by an inflow Mach number of $M = 0.875$. According to the TMR website [24], the reference temperature is set to $T_{ref} = 300K$. The flow field is characterized by a shock located at $x/c \approx 0.66$, inducing separation slightly further downstream at $x/c \approx 0.69$ followed by reattachment at $x/c \approx 1.1$, all measured relative to the leading edge of the bump.

Figure 9 shows a sketch of the computational domain [24]. The numerical computations are carried out on the finest structured grid provided on the TMR website [24], containing $N = 923{,}681$ grid points. At the inflow plane, a turbulence intensity of $Tu_\infty = 0.0089\%$ and a viscosity ratio of $\mu_t/\mu|_\infty = 0.009$ are assumed, following CFL3D defaults.

With TAU, time-accurate computations were required in order to reach a steady state. Since the residuals of the Reynolds stresses leveled-off, the computations were repeated with inflow conditions $Tu_\infty = 0.1\%$ and $\mu_t/\mu|_\infty = 0.1$ according to TAU defaults. With these settings, the Reynolds stress residuals converged by seven orders of magnitude. A comparison of both results did not show any visible differences. Convergence problems were also observed with CFL3D for this case on the fine grid.

The effect of inlet conditions on convergence might be suspected to be related to an observed tendency of Reynolds stress models to predict premature relaminarization in rotating and swirling flows [30, 31]. Nevertheless, since this has been a singular experience within the test cases studied here, no detailed investigation on the underlying reasons for this behavior has been carried out. Hence, no conclusions have been drawn yet on possible improvements of best-practices for running Reynolds stress models.

Figure 10 (left) shows the pressure distributions obtained with the SSG/LRR-ω model with and without the length-scale correction compared to the experimental data by Bachalo and Johnson [29] provided on the TMR website [24]. There is generally good agreement between the TAU and the CFL3D results for the baseline and LSC models, and only minor differences in C_p (the length-scale correction moves the shock very slightly upstream and there is an insignificant shift in the separated region near $x/c = 1$).

Figure 10 (right) shows the predicted skin-friction distributions with and without the length-scale correction. There are no experimental data available except the locations of separation and reattachment. These positions are marked by vertical lines at $x/c = 0.69$ and $x/c = 1.1$. There is generally good agreement between TAU and CFL3D results with some differences in the region downstream of the reattachment point.

Similar to preceding observations, the length-scale correction increases the level of (negative) skin-friction inside the

recirculation zone that is believed to be predicted too low with the standard SSG/LRR-ω model [13, 20]. Furthermore, the length-scale correction moves the reattachment to almost exactly the experimental position. However, separation location is still predicted too early.

Figure 11 shows profiles of the axial mean velocity component and the specific Reynolds shear stress, where the normal coordinate y' is measured from the surface. Predictions by the SSG/LRR-ω model are shown with and without length-scale correction along with the experimental data of Bachalo and Johnson [29]. Only the three most downstream experimental positions are shown, where the influence of the length-scale correction is largest.

There are some differences observed between TAU and CFL3D results, particularly at position $x/c = 1$, but the differences become smaller further downstream. In any case, the influence of LSC on the velocity profiles is limited to a shallow region close to the wall. Clearly, the length-scale correction leads to higher reverse-flow velocity in the recirculation region and slower recovery downstream of the reattachment.

Because the length-scale correction increases the dissipation of turbulence near the wall, the (negative) specific Reynolds-shear stress is slightly reduced compared to the standard model without length-scale correction. In contrast, beyond its extremum there is a slight increase of the (negative) specific Reynolds-shear stress. These observations hold irrespective of the minor differences between the TAU and the CFL3D results.

Figure 12 shows the streamline pattern in the recirculation region according to the TAU solution, where again the streamwise and normal directions have been scaled differently in order to improve the visibility. Obviously, the length-scale correction widens the separation bubble, in particular in the region closest to the separation point. Furthermore, it suppresses the back-bending near reattachment, which is rather strong for this case.

The shaded area, indicating the activity of the length-scale correction, extends from $x/c \approx 0.69$, i.e., just downstream of the predicted separation point, to $x/c \approx 1.9$, i.e., well downstream of the reattachment point.

4. Axisymmetric Separation

Driver [32] has investigated experimentally the flow along a circular cylinder with an externally imposed pressure gradient, causing the flow to separate and reattach. The flow conditions are characterized by a Mach number of $M = 0.08812$ and a Reynolds number of $Re_L = 2 \times 10^6$, based on a unit length of $L = 1m$. According to the TMR website [24], the reference temperature is set to $T_{ref} = 288.9K$.

Figure 13 shows a sketch of the computational domain [24]. The numerical simulations are carried out on the second-finest grid provided on the TMR website [24], containing $N = 137{,}609$ grid points. The pressure gradient is modeled via a streamline-shaped boundary opposite to the cylinder, employing a slip-condition. At the inlet plane, a turbulence intensity of $Tu_\infty = 0.088\%$ and a viscosity ratio of $\mu_t/\mu|_\infty = 0.009$ are assumed, following CFL3D defaults.

Figure 14 shows the pressure and skin friction distributions obtained with the SSG/LRR-ω model with and without length-scale correction compared to the experimental data by Driver [32]. Only very minor differences between TAU

and CFL3D solutions are observed in C_p near its maximum and in c_f downstream of the reattachment point.

As with the flow over the backward-facing step and the NASA-hump, there is virtually no influence of the length-scale correction on the pressure distribution, whereas the skin-friction is sensibly altered. As observed before, in the recirculation zone, the level of negative c_f is slightly increased by the length-scale correction, and the reattachment point moves further downstream, improving the agreement with the experimental data. Nevertheless, the measured minimum c_f is still missed.

Figure 15 shows the streamline pattern in the recirculation according to the TAU solution, where the wall normal direction has been enlarged for improved visibility. Clearly, the length-scale correction increases the size of the separation bubble in terms of length and width. Nevertheless, it is still considerably smaller than observed previously [13] with the models by Spalart and Allmaras [5] and by Menter [6]. Different from the cases investigated before, the length-scale correction is not active within the separation bubble, but in an area slightly above, extending over approximately the complete adverse-pressure gradient region $0 \leq x \leq 0.87m$. Hence, it has only limited influence so that velocity and Reynolds-shear stress profiles are not displayed.

The seemingly different behavior of the length-scale correction compared to the other cases can be attributed to the much smaller size of the separation bubble. With the axisymmetric separation it extends only to approximately 1% of the boundary-layer thickness at the start of the adverse pressure gradient region, whereas the backward-facing step has a height of approximately 38% of the boundary-layer thickness at the step. Therefore, for depicting the separation bubbles, the normal direction had to be stretched much more for the axisymmetric separation than in the other cases, corresponding to a larger magnification of the near-wall region. Indeed, closer inspection shows that, in any of the cases, the length-scale correction is not active in a shallow layer directly at the wall. Whether the results indicate a fundamental difference between geometry and pressure induced separation, as recently found [33], must therefore remain an open question.

V. Conclusion

A length-scale correction term has been developed for the SSG/LRR-ω Reynolds-stress model [7, 8] based on an analysis of the Yap correction [18, 19]. This correction reduces the turbulent length scale in regions where it exceeds the length scale associated with the log-law region of a boundary layer. The term essentially reduces the destruction term of the ω-transport equation, where special care has been taken to avoid a change of sign.

The length-scale correction has been implemented into DLR's unstructured TAU code and NASA's CFL3D code as a modification to the original SSG/LRR-ω model. It has been applied to four different flows from the TMR website [24] involving separation: the subsonic flows over a backward-facing step [25] and over the NASA-hump [26–28], the transonic flow over an axisymmetric bump [29] and the subsonic flow along a cylinder with an imposed adverse pressure gradient [32]. Results show that the length-scale correction is typically active in a region extending from

inside the separation bubble to some distance downstream of the reattachment point, whereas it is inactive in the attached boundary layer of a flat plate.

Very little influence is found on the respective pressure distributions, including the shock position in the investigated transonic flow. In contrast, the length-scale correction is observed to increase the level of negative skin friction in separation bubbles. Nevertheless its effect on velocity and Reynolds-shear stress profiles appears to be limited.

The length-scale correction moves the reattachment point downstream, while maintaining the point of separation. Most notably, it improves the shape of the streamlines near reattachment by removing their unphysical back-bending observed with the original model. For the latter reason, it should be accounted for in future Reynolds-stress model development, in order to avoid misleading conclusions, when comparing predicted reattachment locations to experimental data.

Acknowledgments

Valuable discussions of the first author with Dr. Axel Probst (DLR) are gratefully acknowledged. The second author has been supported by the NASA Transformational Tools and Technologies project under the Revolutionary Computational Aerosciences program.

References

[1] Uzun, A. and Malik, M. R., "Large-Eddy Simulation of Flow over a Wall-Mounted Hump with Separation and Reattachment," *AIAA Journal*, Vol. 56, No. 2, 2018, pp. 715-730.
https://doi.org/10.2514/1.J056397

[2] Spalart, P R., Deck, S., Shur, M. L., Squires, K. D., Strelets, M. K., Travin, A., "A New Version of Detached-eddy Simulation, Resistant to Ambiguous Grid Densities," *Theoretical and Computational Fluid Dynamics*, Vol. 20, No. 3, 2006, pp. 181-195.
https://doi.org/10.1007/s00162-006-0015-0

[3] Lehmkuhl, O., Park, G. I., Bose, S. T., Moin, P., "Large-eddy simulation of practical aeronautical flows at stall conditions," Center of Turbulence Research, Proceedings of the Summer Program 2018, pp. 87-96.

[4] Bush, B., Chyczewski, T., Duraisamy, K., Eisfeld, B., Rumsey, C., and Smith, B., "Recommendations for Future Efforts in RANS Modeling and Simulation," AIAA Paper 2019-0317, San Diego, CA, January 2019.
https://doi.org/10.2514/6.2019-0317

[5] Spalart, P. R. and Allmaras, S. R., "One-Equation Turbulence Model for Aerodynamic Flows," *Recherche Aèrospatiale*, Vol. 1, 1994, pp. 5-21.

[6] Menter, F. R., "Two-Equation Eddy-Viscosity Turbulence Models for Engineering Applications," *AIAA Journal*, Vol. 32, No. 8, 1994, pp. 1598-1605.
https://doi.org/10.2514/3.12149

[7] Eisfeld, B. and Brodersen, O., "Advanced Turbulence Modelling and Stress Analysis for the DLR-F6 Configuration," AIAA Paper 2005-4727, Toronto, Canada, June 2005.
https://doi.org/10.2514/6.2005-4727

[8] Cécora, R.-D-, Radespiel, R., Eisfeld, B., and Probst, A., "Differential Reynolds-Stress Modeling for Aeronautics," *AIAA Journal*, Vol. 53, No. 3, 2015, pp. 739-755.
https://doi.org/10.2514/1.J053250

[9] Speziale, C. G., Sarkar, S., and Gatski, T. B., "Modelling the Pressure-Strain Correlation of Turbulence: an Invariant Dynamical Systems Approach," *Journal of Fluid Mechanics*, Vol. 227, 1991, pp. 245-272.
https://doi.org/10.1017/S0022112091000101

[10] Launder, B. E., Reece, G. J., and Rodi, W., "Progress in the Development of a Reynolds-Stress Turbulence Closure," *Journal of Fluid Mechanics*, Vol. 68, 1975, pp. 537-566.
https://doi.org/10.1017/S0022112075001814

[11] Togiti, V., Eisfeld, B., and Brodersen, O., "Turbulence Model Study for the Flow Around the NASA Common Research Model," *Journal of Aircraft*, Vol. 54, No. 4, 2014, pp. 1331-1343.
https://doi.org/10.2514/1.C032609

[12] Keye, S. and Rudnik, R., "Validation and Assessment of Turbulence Model Impact for Fluid-Structure Coupled Computations of the NASA CRM," 5th CEAS Air & Space Conference, Delft, The Netherlands, Paper No. 103, 7-11 Sept 2015.

[13] Eisfeld, B., Rumsey, C., and Togiti, V., "Verification and Validation of a Second-Moment Closure Model," *AIAA Journal*, Vol. 54, No. 5, 2016, pp. 1524-1541.
https://doi.org/10.2514/1.J054718

[14] Lee-Rausch, E. M., Rumsey, C. L., and Eisfeld, B., "Application of a Full Reynolds Stress Model to High Lift Flows," AIAA Paper 2016-3944, Washington D. C., June 2016.
https://doi.org/10.2514/6.2016-3944

[15] Obi, S., Péric, M., and Scheuerer, G., "A Finite-Volume Calculation Procedure for Turbulent Flows with Second-Order Closure and Colocated Variable Arrangement," *Proc. 7th Symposium on Turbulent Shear Flows*, Stanford University, 1989.

[16] Lasher, W. C. and Taulbee, D. B., "On the Computation of Turbulent Backstep Flow," *International Journal of Heat and Fluid Flow*, Vol. 13, 1992, pp. 30-40.
https://doi.org/10.1016/0142-727X(92)90057-G

[17] Hanjalić, K. and Jakirlić, S., "Contribution Towards the Second-Moment Closure Modelling of Separating Turbulent Flows," *Computers and Fluids*, Vol. 27, No. 2, 1998, pp. 137-156.
https://doi.org/10.1016/S0045-7930(97)00036-4

[18] Yap, J. C., "Turbulent Heat and Momentum Transfer in Recirculating and Impinging Flows," PhD Thesis, University of Manchester, Faculty of Technology, 1987.

[19] Hanjalić, K. and Launder, B., "Modelling Turbulence in Engineering and the Environment," Cambridge University Press, New York, 2011.

[20] Eisfeld, B., Rumsey, C., and Togiti, V., "Verification and Validation of a Second-Moment Closure Model," *AIAA Journal* Erratum, Vol. 54, No. 9, 2016, p. 2926.
https://doi.org/10.2514/1.J055336

[21] Schwamborn, D., Gerhold, T., and Heinrich, R., "The DLR TAU-Code: Recent Applications on Research and Industry," ECCOMAS, 2006.

[22] Krist, S. L., Biedron, R. T., Rumsey, C. L., "CFL3D User's Manual," NASA/TM-1998-208444, June 1998.

[23] Rumsey, C. L., "CFL3D Version 6 [online website]," https://cfl3d.larc.nasa.gov [retrieved 11 April 2019].

[24] Rumsey, C. L., "Turbulence Modeling Resource," https://turbmodels.larc.nasa.gov [retrieved 11 April 2019].

[25] Driver, D. M. and Seegmiller, H. L., "Features of a Reattaching Turbulent Shear Layer in Divergent Channel Flow," *AIAA Journal*, Vol. 23, No. 2, 1985, pp. 163-171.
https://doi.org/10.2514/3.8890

[26] Greenblatt, D., Paschal, K. B., Yao, C.-S., Harris, J., Schaeffler, N. W., and Washburn, A. E., "A Separation Control CFD Validation Test Case, Part 1: Baseline and Steady Suction," *AIAA Journal*, Vol. 44, No. 12, 2006, pp. 2820-2830.
https://doi.org/10.2514/1.13817

[27] Greenblatt, D., Paschal, K. B., Yao, C.-S., and Harris, J., "A Separation Control CFD Validation Test Case, Part 2: Zero Efflux Oscillatory Blowing," *AIAA Journal*, Vol. 44, No. 12, 2006, pp. 2831-2845.
https://doi.org/10.2514/1.19324

[28] Naughton, J. W., Viken, S. A., and Greenblatt, D., "Skin-Friction Measurements on the NASA Hump Model," *AIAA Journal*, Vol. 44, No. 6, 2006, pp. 1255-1265.
https://doi.org/10.2514/1.14192

[29] Bachalo, W. D. and Johnson, D. A., "Transonic, Turbulent Boundary-Layer Separation Generated on an Axisymmetric Flow Model," *AIAA Journal*, Vol. 24, No. 3, 1986, pp. 437-443.
https://doi.org/10.2514/3.9286

[30] Jakirlić, S., Hanjalić, K., Tropea, C., "Modeling Rotation and Swirling Turbulent Flows: A Perpetual Challenge," *AIAA Journal*, Vol. 40, No. 10, 2002, pp. 1984-1996.
https://doi.org/10.2514/2.1560

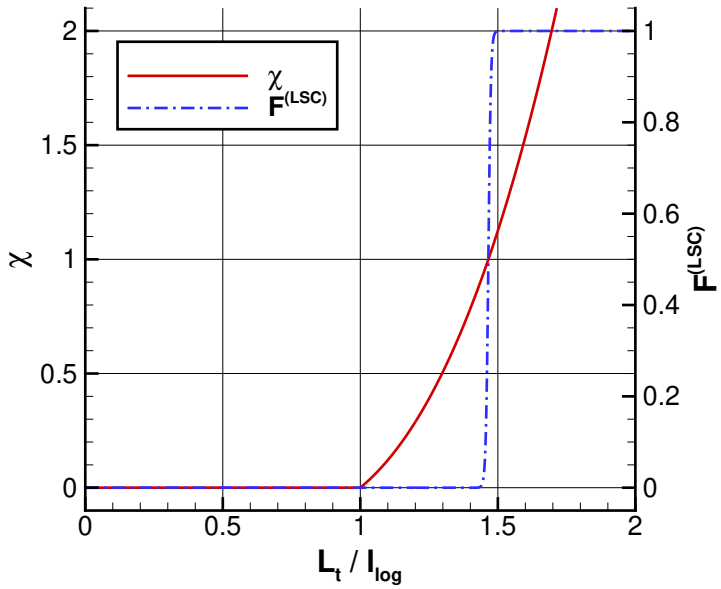

Fig. 1 Parameter χ for modifying the ω-destruction term according to the Yap correction and length-scale correction function $F^{(LSC)}(\chi)$, both plotted versus the length-scale ratio $\mathcal{L}_t/\ell_{\log}$.

[31] Ashton, N., Davis, J., Brehm, C., "Assessment of the Elliptic Blending Reynolds Stress Model for a Rotating Turbulent Pipe Flow Using New DNS Data," AIAA Paper 2019-2966, AIAA Aviation Forum, Dallas, TX, June 2019. https://doi.org/10.2514/6.2019-2966

[32] Driver, D. M., "Reynolds Shear Stress Measurements in a Separated Boundary Layer Flow," AIAA Paper 91-1787, Honolulu, HI, June 1991. https://doi.org/10.2514/6.1991-1787

[33] Abe, H., "Reynolds-number dependence of wall-pressure fluctuations in a pressure-induced turbulent separation bubble," *Journal of Fluid Mechanics*, Vol. 833, 2017, pp. 563-598. https://doi.org/10.1017/jfm.2017.694

[34] Wilcox, D. C., "Reassessment of the Scale Determining Equation for Advanced Turbulence Models," *AIAA Journal*, Vol. 26, No. 11, 1988, pp. 1299-1310. https://doi.org/10.2514/3.10041

[35] Launder, B. E. and Sharma, B. I., "Application of the Energy-Dissipation Model of Turbulence to the Calculation of Flow Near a Spinning Disc," *Letters in Heat and Mass Transfer*, Vol. 1, 1974, pp. 131-138. https://doi.org/10.1016/0094-4548(74)90150-7

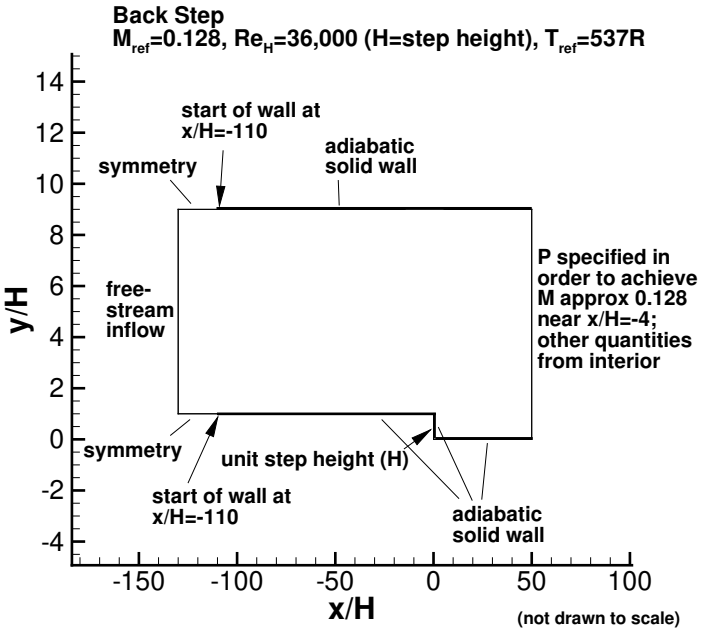

Fig. 2 Backward-facing step. Sketch of the computational domain [24].

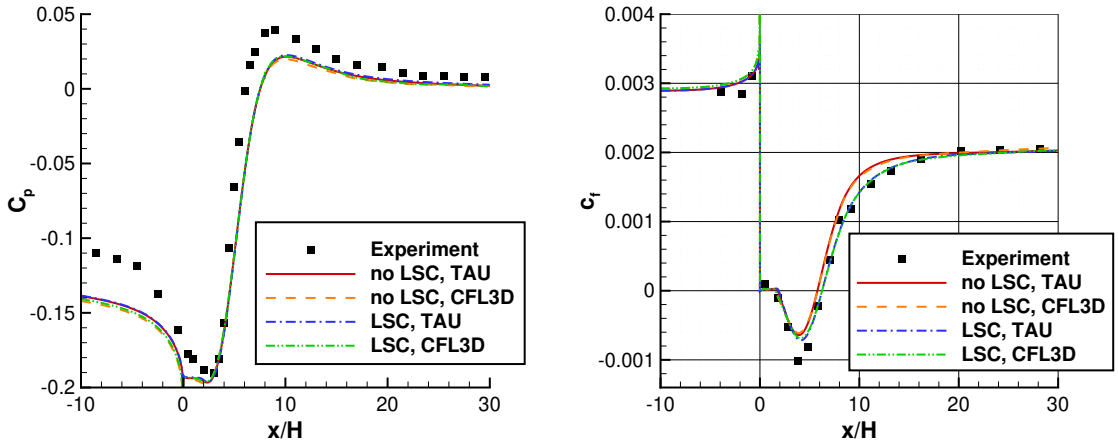

Fig. 3 Backward-facing step. Pressure distribution (left) and skin-friction distribution (right). SSG/LRR-ω with and without length-scale correction (LSC) compared to experimental data by Driver and Seegmiller [25].

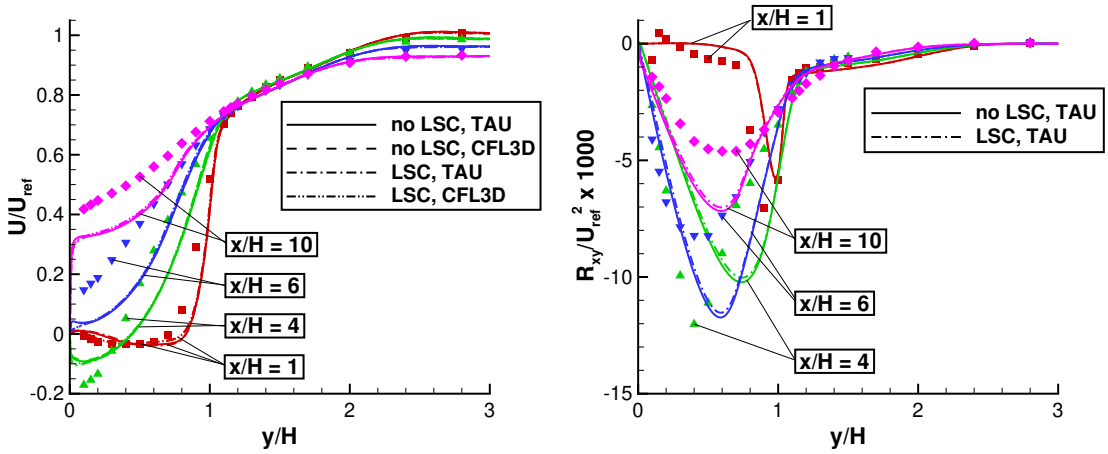

Fig. 4 Backward-facing step. Velocity profiles (left) and Reynolds-shear stress profiles (right). SSG/LRR-ω with and without length-scale correction (LSC) compared to experimental data by Driver and Seegmiller [25] (symbols).

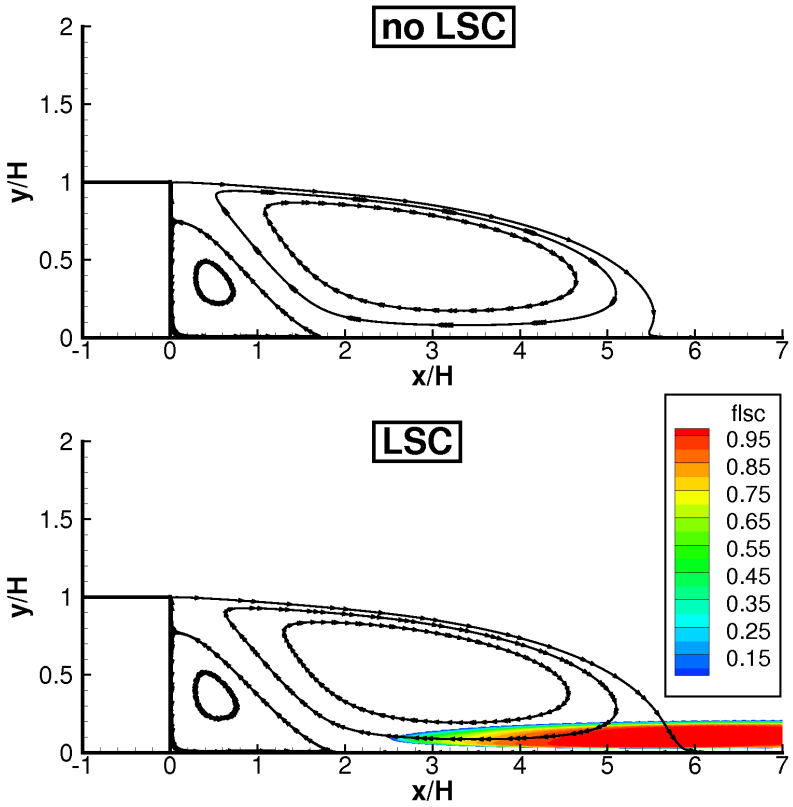

Fig. 5 Backward-facing step. Recirculation region with and without length-scale correction. Shaded area indicates level of $F^{(LSC)}$. Steady-state TAU solution.

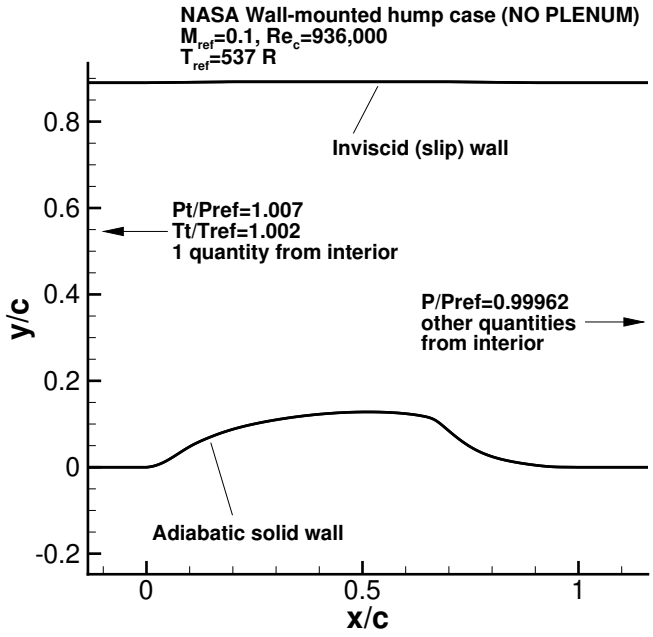

Fig. 6 NASA-hump. Sketch of the geometry and boundary conditions [24].

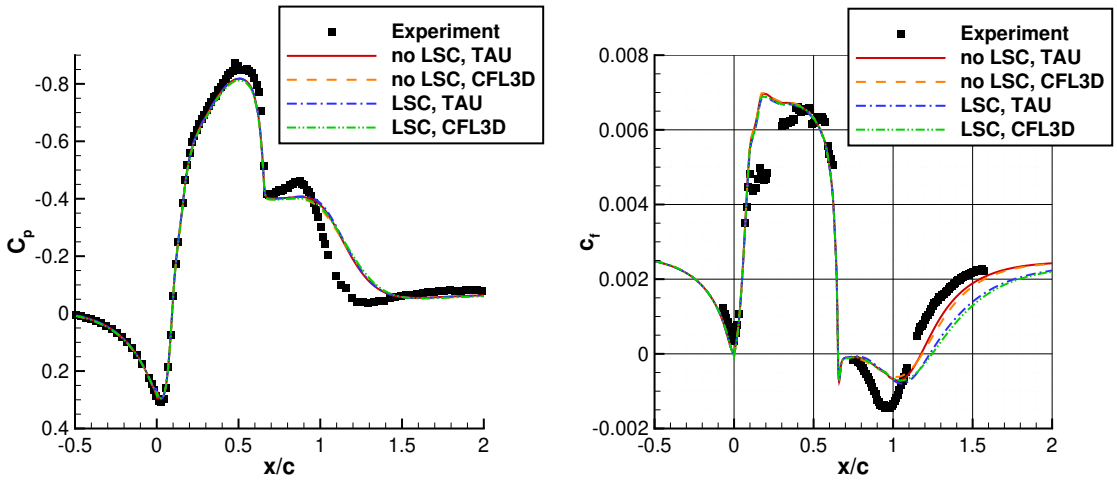

Fig. 7 NASA-hump. Pressure distribution (left) and skin-friction distribution (right). SSG/LRR-ω with and without length-scale correction (LSC) compared to experimental data by Greenblatt et al. [26–28].

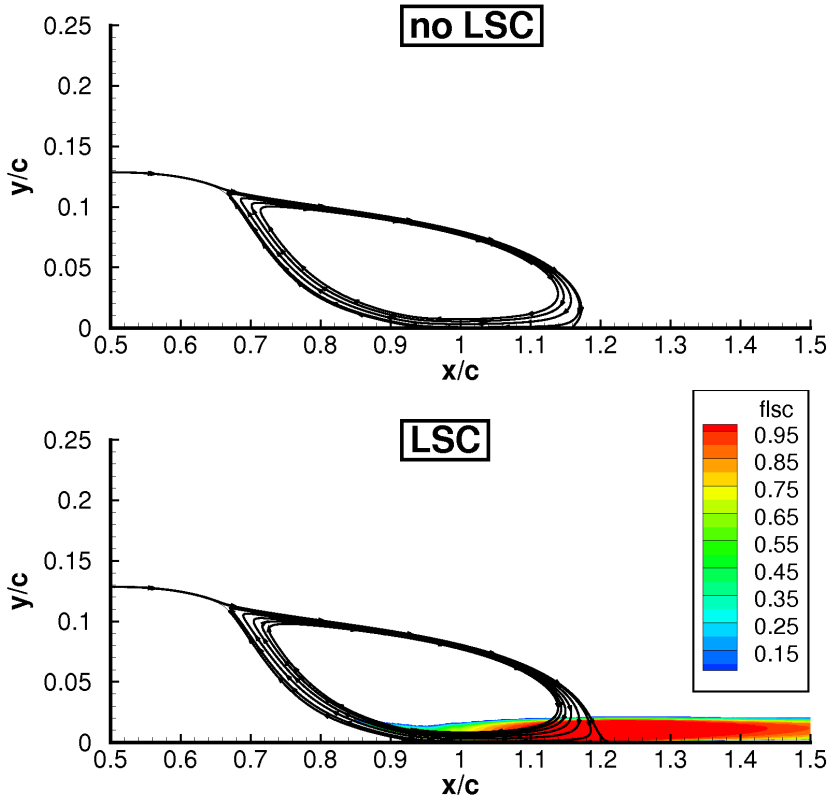

Fig. 8 NASA-hump. Recirculation region with and without length-scale correction. Shaded area indicates level of $F^{(LSC)}$. TAU solution.

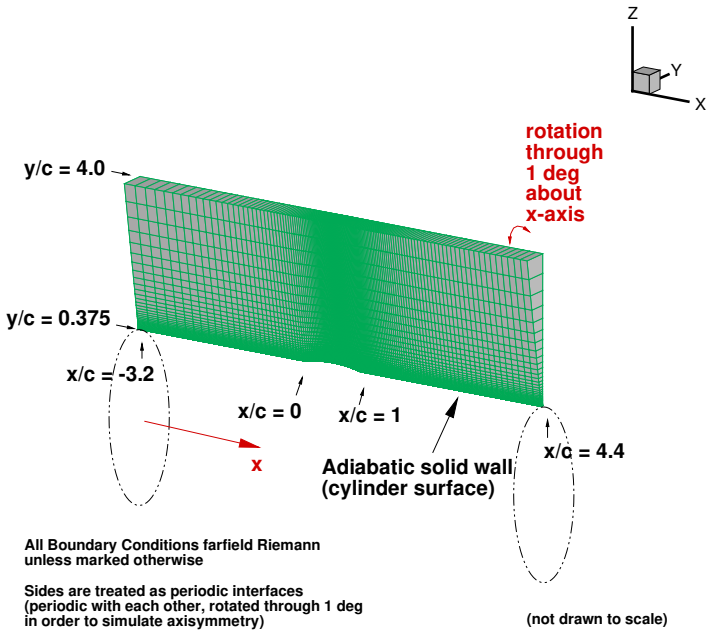

Fig. 9 Axisymmetric bump. Sketch of the computational domain [24].

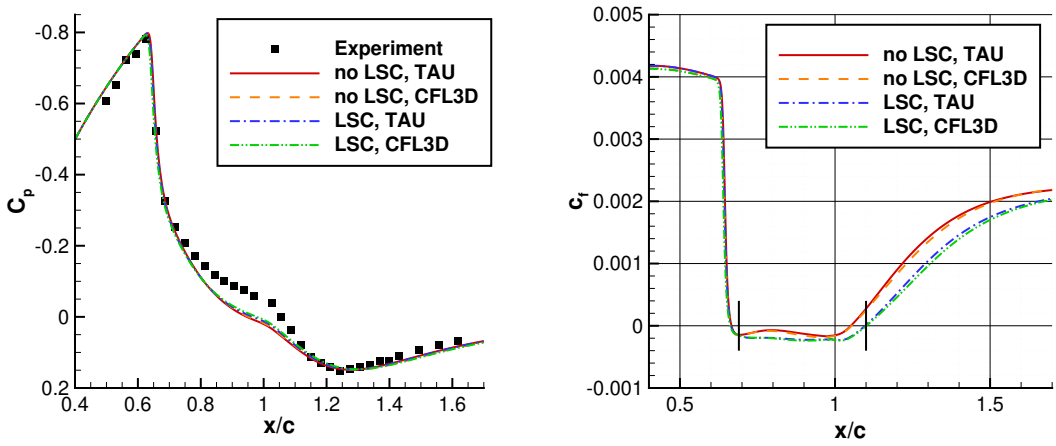

Fig. 10 Axisymmetric bump. Pressure distribution (left) and skin-friction distribution (right). SSG/LRR-ω with and without length-scale correction (LSC) compared to experimental data by Bachalo and Johnson [29].

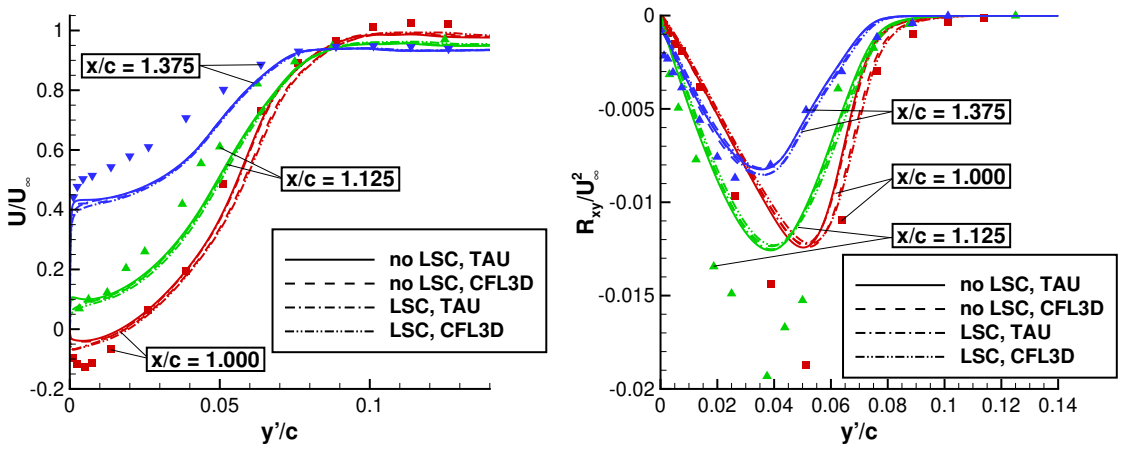

Fig. 11 Axisymmetric bump. Velocity profiles (left) and Reynolds-shear stress profiles (right). SSG/LRR-ω with and without length-scale correction (LSC) compared to experimental data by Bachalo and Johnson [29] (symbols).

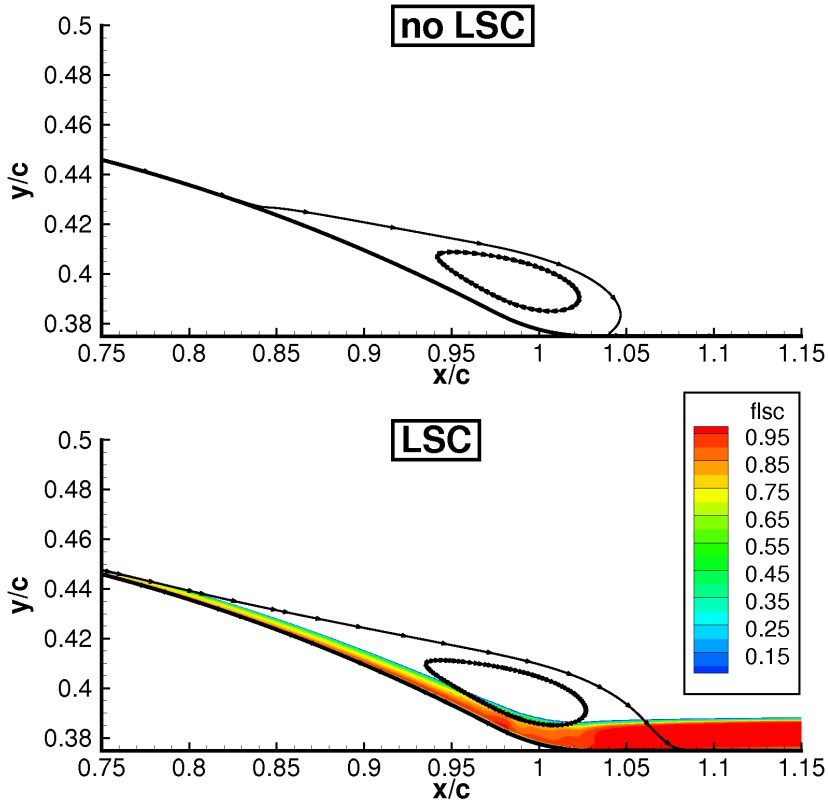

Fig. 12 Axisymmetric bump. Recirculation region with and without length-scale correction. Shaded area indicates level of $F^{(LSC)}$. TAU solution.

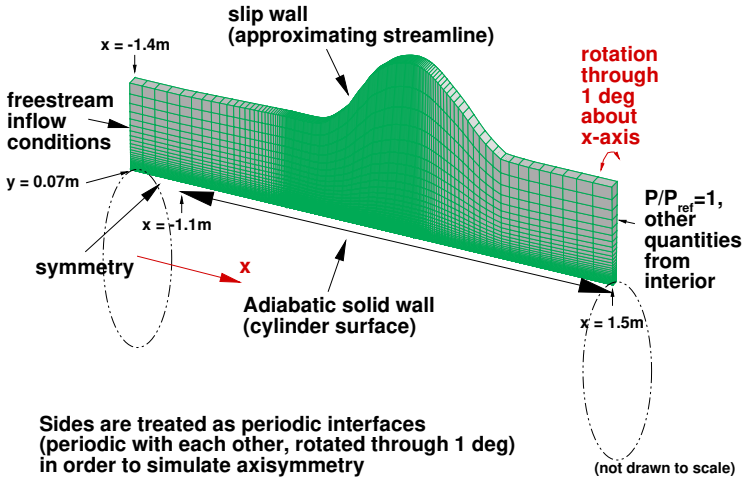

Fig. 13 Axisymmetric separation. Sketch of the computational domain [24].

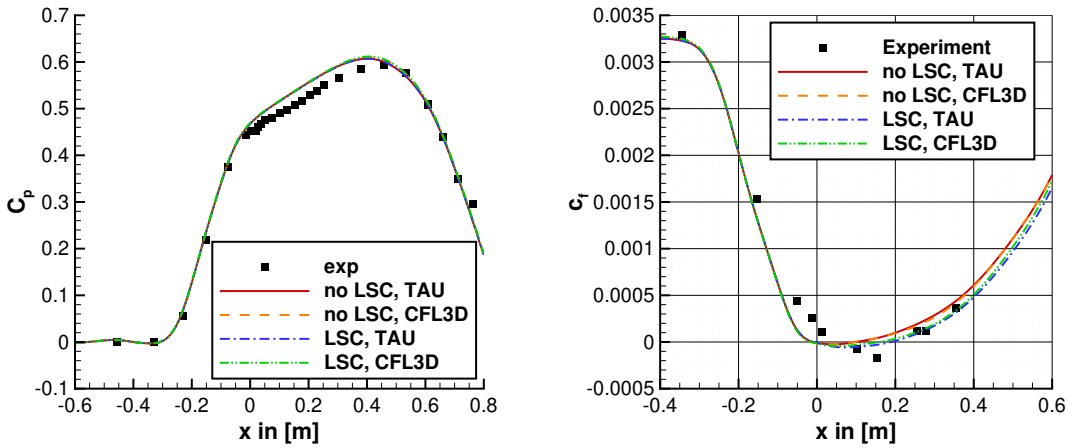

Fig. 14 Axisymmetric separation. Pressure distribution (left) and skin-friction distribution (right). SSG/LRR-ω with and without length-scale correction (LSC) compared to experimental data by Driver [32].

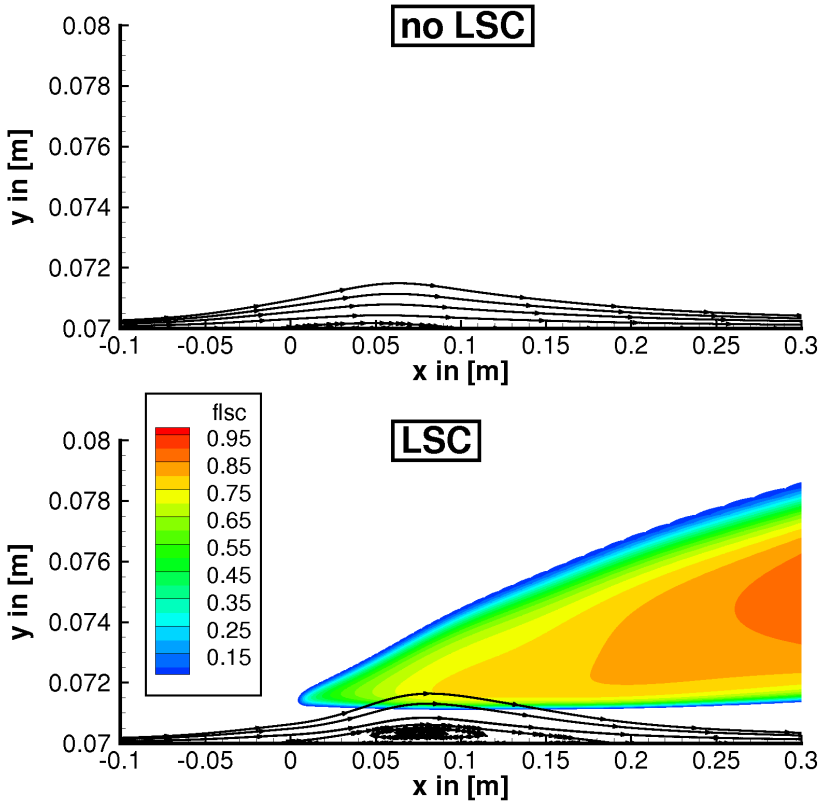

Fig. 15 Axisymmetric separation. Recirculation region with and without length-scale correction. Shaded area indicates level of $F^{(LSC)}$. TAU solution.

A. SSG/LRR-ω Model

A. Reynolds Stress Transport Equation

The SSG/LRR-ω model [13, 20] employs the Reynolds stress transport equation

$$\frac{\partial\left(\rho R_{ij}\right)}{\partial t}+\frac{\partial}{\partial x_k}\left(\rho R_{ij}U_k\right)=\rho P_{ij}+\rho\Pi_{ij}-\rho\epsilon_{ij}+\rho D_{ij} \tag{17}$$

with ρ the mean density, U_i the mean velocity components and ρR_{ij} the Reynolds stresses.

The terms on the right-hand side are:

- Production

$$\rho P_{ij}=-\rho R_{ik}\frac{\partial U_j}{\partial x_k}-\rho R_{jk}\frac{\partial U_i}{\partial x_k} \tag{18}$$

- Pressure-strain correlation

$$\begin{aligned}\rho\Pi_{ij} &= -\left(C_1\rho\epsilon+\frac{1}{2}C_1^*\rho P_{kk}\right)b_{ij}+C_2\rho\epsilon\left(b_{ik}b_{kj}-\frac{1}{3}b_{kl}b_{kl}\delta_{ij}\right)\\ &\quad+\left(C_3-C_3^*\sqrt{b_{kl}b_{kl}}\right)\rho kS_{ij}^*\\ &\quad+C_4\rho k\left(b_{ik}S_{jk}+b_{jk}S_{ik}-\frac{2}{3}b_{kl}S_{kl}\delta_{ij}\right)\\ &\quad+C_5\rho k\left(b_{ik}W_{jk}+b_{jk}W_{ik}\right),\end{aligned} \tag{19}$$

with $k=R_{ii}/2$ the specific kinetic turbulence energy and

$$b_{ij}=\frac{R_{ij}}{2k}-\frac{1}{3}\delta_{ij} \tag{20}$$

the anisotropy of Reynolds stresses.

Velocity gradients enter via strain rates

$$S_{ij}=\frac{1}{2}\left(\frac{\partial U_i}{\partial x_j}+\frac{\partial U_j}{\partial x_i}\right), \tag{21}$$

traceless strain rates

$$S_{ij}^*=S_{ij}-\frac{1}{3}S_{kk}\delta_{ij}, \tag{22}$$

and rotation rates

$$W_{ij}=\frac{1}{2}\left(\frac{\partial U_i}{\partial x_j}-\frac{\partial U_j}{\partial x_i}\right). \tag{23}$$

The C_i and C_i^* are model coefficients.

- Dissipation

$$\rho\epsilon_{ij} = \frac{2}{3}\rho\epsilon, \tag{24}$$

with the isotropic dissipation rate

$$\epsilon = c_\mu k\omega, \tag{25}$$

and $c_\mu = 0.09$. The specific dissipation rate ω is provided by Menter's baseline equation given below.

- Diffusion

$$\rho D_{ij} = \frac{\partial}{\partial x_k}\left[\left(\mu\delta_{ij} + D^{(GD)}\frac{\rho k R_{kl}}{\epsilon}\right)\frac{\partial R_{ij}}{\partial x_l}\right], \tag{26}$$

with μ the mean dynamic fluid viscosity and $D^{(GD)}$ a model coefficient.

B. ω-Transport Equation

The ω-transport equation is based on Menter's baseline equation [6]

$$\frac{\partial(\rho\omega)}{\partial t} + \frac{\partial}{\partial x_k}(\rho\omega U_k) = \rho P^{(\omega)} - \rho\Phi^{(\omega)} + \rho D^{(\omega)} + \rho C_D^{(\omega)} \tag{27}$$

with the following terms on the right hand side:

- ω-production

$$\rho P^{(\omega)} = \alpha\frac{\omega}{k}\frac{\rho P_{kk}}{2}. \tag{28}$$

with α a model coefficient

- ω-destruction

$$\rho\Phi^{(\omega)} = \beta\left[1 - F^{(LSC)}(\chi)\right]\rho\omega^2 \tag{29}$$

with β a model coefficient.

The length-scale correction is given by

$$F^{(LSC)}(\chi) = \frac{1}{2}\left\{1 + \tanh\left[A\left(\chi - \chi_T\right)\right]\right\} \tag{30}$$

with argument

$$\chi = \max\left[\left(\frac{\mathcal{L}_t}{\ell_{log}} - 1\right)\left(\frac{\mathcal{L}_t}{\ell_{log}}\right)^2, 0\right], \tag{31}$$

the length-scale ratio

$$\frac{\mathcal{L}_t}{\ell_{log}} = \frac{k^{1/2}}{c_\mu^{1/4}\kappa\omega d}, \tag{32}$$

the von Kármán constant $\kappa = 0.41$ and the wall distance d. The parameters are set to $\chi_T = 1$ and $A = 31$. Note

Table 2 Bounding Values of the SSG/LRR-ω Model Term Coefficients ($c_2^{(LRR)} = 0.52$).

	C_1	C_1^*	C_2	C_3	C_3^*	C_4	C_5	$D^{(GD)}$
$\phi^{(\varepsilon)}$	3.4	1.8	4.2	0.8	1.3	1.25	0.4	0.22
$\phi^{(\omega)}$	3.6	0	0	0.8	0	$\frac{18c_2^{(LRR)}+12}{11}$	$\frac{-14c_2^{(LRR)}+20}{11}$	$0.75c_\mu$

that the length-scale correction requires the proper wall distance d, which, in a numerical method, is generally *not* equivalent to the distance to the nearest grid point or cell center on the wall.

For $F^{(LSC)} = 0$, Menter's original baseline equation [6] is retrieved, corresponding to the standard SSG/LRR-ω model without length-scale correction.

- ω-diffusion

$$\rho D^{(\omega)} = \frac{\partial}{\partial x_k}\left[\left(\mu + \sigma_\omega \frac{\rho k}{\omega}\right)\frac{\partial \omega}{\partial x_k}\right] \tag{33}$$

with σ_ω a model coefficient.

- Cross-diffusion

$$\rho C_D^{(\omega)} = \sigma_d \frac{\rho}{\omega} \max\left(\frac{\partial k}{\partial x_k}\frac{\partial \omega}{\partial x_k}, 0\right) \tag{34}$$

with σ_d a model coefficient.

C. Model Coefficients

All model coefficients $\phi = C_1, C_1^*, C_2, C_3, C_3^*, C_4, C_5, D^{(GD)}, \alpha, \beta, \sigma_\omega, \sigma_d$ are blended according to

$$\phi = F_1 \phi^{(\omega)} + (1 - F_1)\,\phi^{(\epsilon)} \tag{35}$$

between the bounding values associated with the ω-equation by Wilcox [34] near walls ($F_1 = 1$) and the standard ϵ-equation [35] at the boundary layer edge ($F_1 = 0$). The blending function is given by [6]

$$F_1 = \tanh\left(\zeta^4\right) \tag{36}$$

with the argument

$$\zeta = \min\left[\max\left(\frac{\sqrt{k}}{c_\mu \omega d}, \frac{500\mu}{\rho \omega d^2}\right), \frac{4\sigma_\omega^{(\varepsilon)} \rho k}{\sigma_d^{(\varepsilon)} \frac{\rho}{\omega} \max\left(\frac{\partial k}{\partial x_k}\frac{\partial \omega}{\partial x_k}, 0\right) d^2}\right]. \tag{37}$$

The bounding values of the coefficients are given in Table 2 for the terms of the Reynolds-stress transport equation and in Table 3 for the ω-transport equation.

Table 3 Bounding Values of ω-Transport Equation Coefficients.

	α	β	σ_ω	σ_d
$\phi^{(\varepsilon)}$	0.44	0.0828	0.856	1.712
$\phi^{(\omega)}$	0.5556	0.075	0.5	0

D. Boundary Conditions

1. Far Field

Isotropic turbulence

$$R_{ij}\Big|_\infty = \frac{2}{3} k_\infty \delta_{ij} \tag{38}$$

with prescribed values for k_∞ and ω_∞. A turbulence intensity

$$Tu_\infty = \frac{\sqrt{\frac{2}{3}k_\infty}}{U_\infty} \tag{39}$$

and a viscosity ratio

$$\frac{\mu_t}{\mu}\bigg|_\infty = \frac{\rho_\infty\, k_\infty}{\omega_\infty\, \mu_\infty} \tag{40}$$

might be employed.

2. Solid Wall

No-slip condition

$$R_{ij}\Big|_w = 0. \tag{41}$$

Extrapolation according to Menter [6]

$$\omega_w = F \frac{6\mu_w}{\rho_w \beta d_1^2} \tag{42}$$

with $\beta = 0.075$ the near-wall value in Table 3, d_1 the wall distance of the nearest field point and extrapolation factor $F = 10$.